

# Mass and Heat Transport During Anti-icing and De-icing Processes

SHANG Yuhe<sup>1,2,3</sup>, LI Dong<sup>1,2,3\*</sup>, WANG Jiayong<sup>1</sup>,  
SHEN Leihu<sup>1</sup>, AI Fanbiao<sup>1</sup>, WU Jiulong<sup>1</sup>

1. School of Energy and Mechanical Engineering, Nanjing Normal University, Nanjing 210046, P.R.China;

2. Jiangsu Energy System Process Conversion and Emission Reduction Technology Engineering Laboratory, Nanjing Normal University, Nanjing 210046, P.R.China;

3. Key Laboratory of Icing and Anti/De-icing, China Aerodynamics Research and Development Center, Mianyang 621000, P.R.China

(Received 10 March 2023; revised 15 June 2023; accepted 10 August 2023)

**Abstract:** Suppression of ice formation by inhibiting droplet deposition from both passive surface functionalization and active application of ultrasonic vibration is investigated through numerical simulation and experiments. The contact time of droplet impacting on superhydrophobic surfaces with macro-structures, including cubic protrusion, single and crossed triangular ridges, and suspended prism, can be effectively reduced due to the droplet deformation induced by the structures during expansion and retraction processes. The substrate subjected to ultrasonic vibration exhibits a nonlinear distribution of equivalent shear stress, which leads to different dynamics modes of impact droplet and iced droplet removal performance. This work reveals the effectiveness of macro-structures and the ultrasonic vibration on anti-icing and de-icing, and provides potential approaches for the design and optimization of anti-/de-icing system.

**Key words:** anti-icing; de-icing; droplet impact; ultrasonic vibration; superhydrophobic surface; macro-structure; de-frosting

**CLC number:** TK11

**Document code:** A

**Article ID:** 1005-1120(2023)S1-0066-18

## 0 Introduction

Unwanted ice, often builds up on the edges of aircraft surfaces like the wings, tail and even the engines, with surface thickness and roughness similar to coarse sandpaper reduces lift by over 30% and at the same time increases drag by  $\sim 40\%$ <sup>[1-2]</sup>. Icing also increases the weight of the aircraft<sup>[3]</sup>. This, together with the extra drag, can increase the overall fuel consumption of the aircraft and may cause severe flight accident<sup>[4]</sup>. Therefore, the need to inhibit ice formation and remove ice to improve the energy-saving and all-weather flying safety is absolutely necessary.

Anti-icing systems are designed for activation before the aircraft enters icing conditions to prevent

the formation of ice. The emerging icephobic surface has received much attention for its remarkable ability in passive ice suppression<sup>[5-8]</sup>. The icephobic surfaces<sup>[9-10]</sup>, including superhydrophobic surfaces<sup>[5, 11]</sup>, slippery surfaces<sup>[12-14]</sup> and other aqueous materials<sup>[15]</sup>, serve as the unwettable substrates that reject droplet deposition and hence inhibit ice formation. Compared to the freezing deposition on the untreated surface, the droplets impacting on the superhydrophobic surface can quickly bounce away, and consequently inhibit the formation of the ice nuclei<sup>[16-17]</sup>. To further enhance the droplet transport, macro-structures have been added on the superhydrophobic surface.

The wire cut the impacting droplet into several pieces and the decrease of contact time was in direct

\*Corresponding author, E-mail address: 62084@njnu.edu.cn.

**How to cite this article:** SHANG Yuhe, LI Dong, WANG Jiayong, et al. Mass and heat transport during anti-icing and de-icing processes[J]. Transactions of Nanjing University of Aeronautics and Astronautics, 2023, 40(S1): 66-83.

<http://dx.doi.org/10.16356/j.1005-1120.2023.S1.007>

proportion to the number the split sub-droplets<sup>[18]</sup>. Gauthier et al.<sup>[19]</sup> added a single superhydrophobic wire of different diameters on the superhydrophobic surface, and the experiments demonstrated that the droplet would split into multiple pieces when it rebounded, and the decrease in contact time was associated with the number of sub-droplet split. The maximum reduction in contact time can reach 44% in the high-impact velocity regime. Shen et al.<sup>[20]</sup> increased the number of macrostructures to eight and found that the minimum contact time was the spreading time of the droplet. Similar phenomena and conclusions on the contact time reduction were reported in experiments and numerical simulations of droplet impacting on superhydrophobic surfaces with different types of macro-structures like cylinder, triangular prism, sphere and other combined complex structures. Regulagadda et al.<sup>[21]</sup> added triangular cross section micropillar protrusions on the superhydrophobic surface and found that the impacting droplet dynamic behavior and the contact time would be reduced by up to 40%. Hu et al.<sup>[22]</sup> studied the influences of the eccentric distance on the contact time of and the droplet dynamic behavior of the eccentric droplet impacting on the single-ridge superhydrophobic surfaces. The experiment investigated that the dynamic behavior and the contact time depended on the eccentric distance and the Weber number ( $We$ ), and the contact time could be reduced by about 30%<sup>[23]</sup>. The dynamics of water droplets remarkably changed during impacting on the superhydrophobic polyethylene surfaces with rectangle, semicircle, and triangle macrostructures<sup>[24]</sup>. The elimination of the retraction process of droplet caused the quick rebound to decrease the contact time of droplet significantly<sup>[25]</sup>. Considering the difficulty of obtaining the internal details of the flow field in experimental research, simulation research is also widely developed in the droplet impacting study. Liu et al.<sup>[26]</sup> studied the droplet impacting on a semi-cylinder through experiments and a lattice Boltzmann method (LBM). They found that more momentum was transferred into radial direction than the axial direction, which led to the asymmetry of the spreading and retraction process,

and the contact time was reduced by about 40%. Andrew et al.<sup>[27]</sup> simulated a droplet impacting on cylinders with different radiuses and found that when the droplet radius and the cylinder radius are close, the contact time is decreased by about 35%. Chantelot et al.<sup>[28]</sup> studied the droplet impacting on superhydrophobic surfaces with dot-like macrostructures through both experiments and numerical simulation. The central part of the liquid film was pierced by the microstructures, and hence, the droplet rebounded from the surface in the form of ring and the contact time by approximately 52%. Lin et al.<sup>[29]</sup> simulated the process of a droplet impacting on a superhydrophobic surface with a single rectangular. The width and height of the rectangle and the variation in  $We$  would cause different rebounding processes, and the contact time was reduced by about 48%. Lin et al.<sup>[30]</sup> simulated two identical droplets simultaneously impacting the superhydrophobic surface and found that the spreading and retracting process got asymmetric owing to the macroscopic structure, and the droplets formed. From both experimental and numerical results, the decorated superhydrophobic surfaces presented an obvious improvement in the droplet transportability and contact time reduction. To be a potential way of enhancing droplet mobility to inhibit impacting droplet ice formation<sup>[31]</sup>, detailed study on the droplet spreading, retraction and break-up dynamics and the mechanism of contact time reduction for different types of macro-structure still need to advance.

Beside the passive anti-icing methods, the auxiliary method that adopting ultrasonic vibration, as an active de-icing method, has attracted much interest due to its prominent effect on ice removal<sup>[32-33]</sup>. The high-frequency vibration and the interface shear force caused by ultrasonic wave on the solid substrate cause the adhesive linkage between the ice and the cold substrate to loosen, which has been verified by experiments<sup>[34]</sup>. The de-icing performance depends on the average shear stress and total energy density of the ultrasonic wave as well as the ice structure<sup>[35-37]</sup>. Some other work has been done to analyze the mechanism of droplet atomization and removal dynamics by capillary wave<sup>[38-41]</sup>. The drop-

let breakup can be controlled by the viscous-inertia balance that initiated by the capillary wave at the liquid-vapor interface via Faraday excitation. The droplet presenting ejection from the breakup of transient liquid spikes is generated by the localized collapse of free-surface waves. The droplet can also be atomized by the ultrasonic wave because that the spike forms firstly on the droplet surface due to the impingement of the liquid flowing. The sub-droplet ejected from the droplet surface is determined by the velocity difference between the leading and tail of the spike<sup>[42]</sup>.

The ultrasound has also been used in the deicing field<sup>[43-44]</sup>. The experiments on wind turbine blade, fiber reinforced composite, helicopter blade and so forth demonstrated the feasibility of ultrasound on ice sheet removal<sup>[44-46]</sup>. Both experiments and numerical results revealed that the horizontal shear force triggered by the ultrasonic wave played a key role in ice shedding, which depended on the frequency and power of the transducer<sup>[47-50]</sup>.

Ultrasonic, as a new and potential energy-efficient anti-/de-icing technique, has raised the increasing interest with its energy-saving effect, low running costs, good applicability and environmental conservation. Despite the achievements on the removal effect of sessile droplet or ice sheet by the ultrasonic vibration, the ice formed by the impacting droplet deposition, which is more common in real industrial applications, is rarely studied. In this study, we report our accumulated work on droplet manipulation by means of surface functionalization and ultrasonic vibration facilitation. Detailed analysis is provided from both numerical simulation and experiments results. We carefully compared the results and revealed the effectiveness of ultrasonic vibration on droplet manipulation and its deicing performance.

## 1 Anti-icing

### 1.1 Droplet impact dynamics on macro-structure decorated superhydrophobic surfaces

To systematically investigate the droplet dy-

namics of impacting on the macro-structure decorated superhydrophobic surfaces, we designed our study from the view of the protrusion geometry. From 0-D structure, the cube, to 1-D structure, the triangle ridge, then to the 2-D structure, the multi-crossed ridge, finally to the 3-D structure, the suspended octagonal prism (macro-structures see Fig.1). The increment in the macro-structure dimensionality resulted in different droplet dynamics but all presented the contact time reduction.

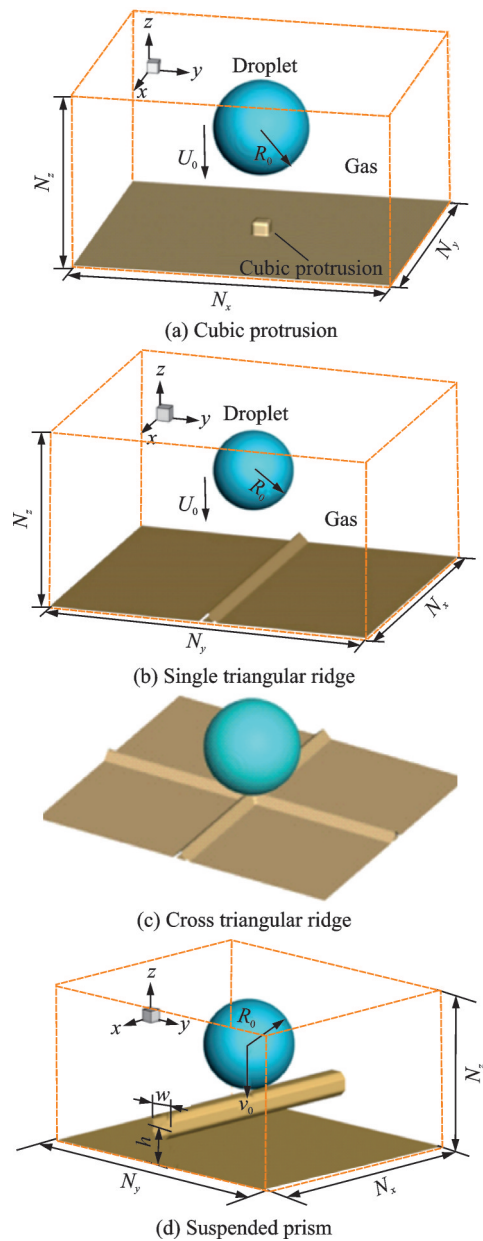


Fig.1 Schematic diagram of superhydrophobic surface with macro-structure

#### 1.1.1 Cubic protrusion

Droplet impact dynamics on a superhydrophobic surface with a cubic protrusion (the edge length

$d=6$  mm) was simulated by the LBM and the contact time reduction mechanism was explored. In addition, the droplet bouncing behavior was analyzed with the effect of a wide range of Weber number ( $We=18.28-106.77$ ). Three distinct droplet bouncing modes can be observed due to the cubic protrusion. At the low region of  $We$ , a bouncing with no ring formation mode can be seen with incomplete retraction (Figs.2(a, b)). For the moderate region of  $We$  from 43.45 to 67.16, a bouncing with ring formation and disappearance modes is accompanied with unbalanced droplet dynamics and accelerated incomplete retraction. As  $We$  exceeds 67.16, a bouncing with ring formation is observed owing to the inner and outer rim colliding in opposite directions.

Under the condition of  $We$  between 18.28 and

43.45, the contact time decreases linearly with an approximately 28.85%—37.42% reduction compared with a droplet impacting on a flat superhydrophobic surface. As the  $We$  varies from 43.45 to 106.77, two plateaus are observed in the presence of the cubic protrusion with approximately 38% and 57.31% contact time reduction, respectively, for moderate and high  $We$ . Aside from that, the spreading time of the droplet outer rim is independent of  $We$ . Hence, the contact time reduction mainly depends on the retraction process. The retraction degree can be weakened with increasing  $We$  owing to the liquid ring formation, which is attributed to puncture by the cubic protrusion.

Fig.2(c) shows the variations of the spreading time and retraction time of the outer and inner rims

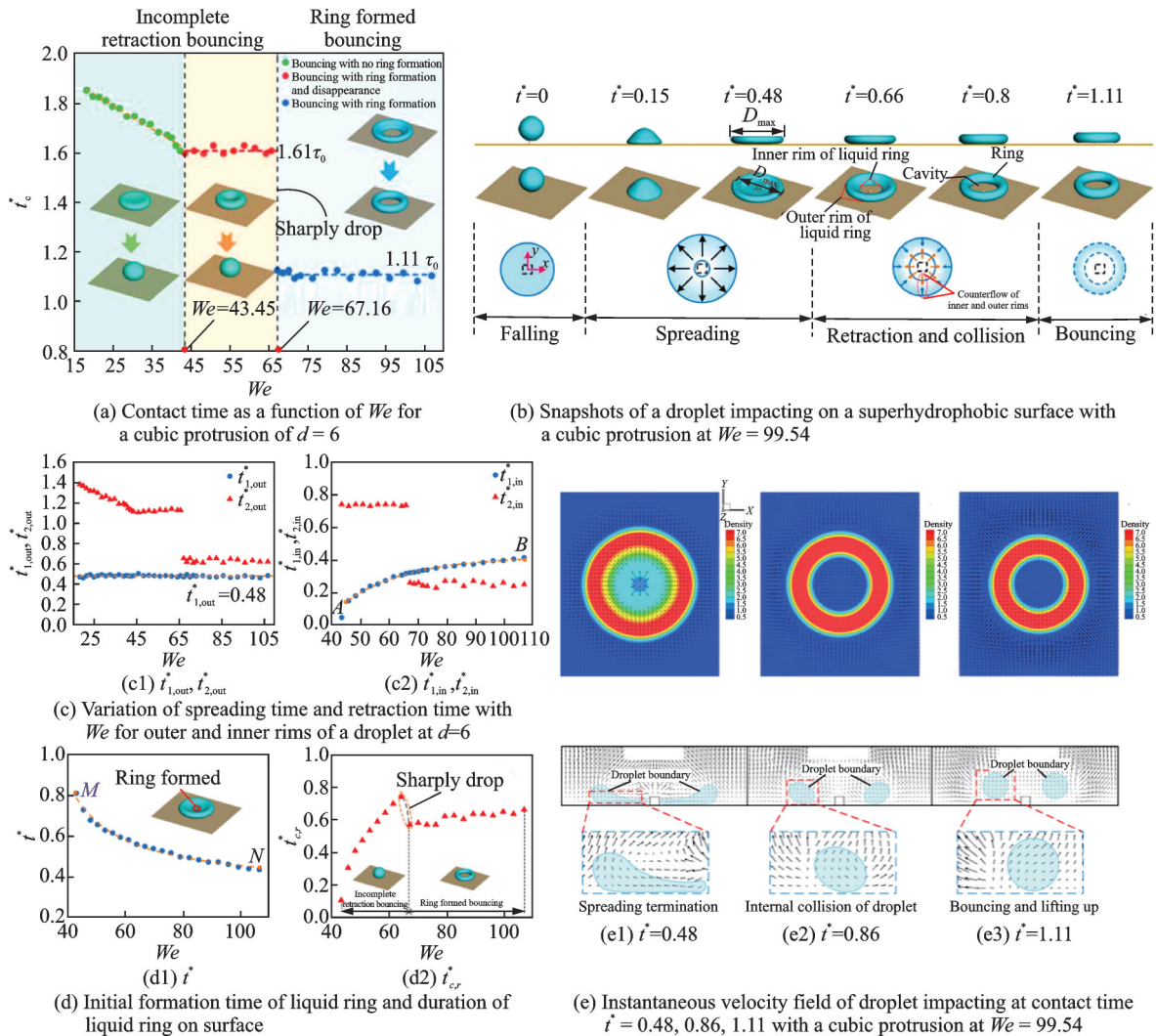


Fig.2 Dynamic behavior of a droplet impacting on superhydrophobic surface with cubic protrusion

of the droplet. The spreading time of the outer rim is independent of  $We$  in a large range, and the retraction time of the outer rim first decreases and then stabilizes at 1.123 and 0.626. The spreading time of the inner rim of the liquid ring, which starts at  $We = 43.45$ , increases at a slower rate rather than reaching a stable value as  $We$  increases. It should be noted that the retraction time of the inner rim tends to be stable and drops dramatically due to the rebounding mode transformation after the critical  $We = 67.16$ . In Fig.2(d), the initial formation time of the liquid ring reveals that the increase in  $We$  can lead to an earlier puncture time of the droplet. In contrast, in the moderate range of  $We$ , the duration of the liquid ring increases with  $We$ , because the liquid ring appears and then disappears in the process. However, after  $We = 67.16$ , the droplet will bounce off the superhydrophobic surface as a ring, which results in a significant reduction in the duration of the liquid ring on the surface.

To further elaborate the mechanism, vertical views and cross sections of the instantaneous velocity field of a droplet impacting on the superhydrophobic surface with the cubic protrusion at  $We = 99.54$  are revealed in Fig.2(d). The collision of the inward flow from the outer rim and outward flow from the inner rim generate an upward motion.

A symmetrical dynamic behavior during due to the cubic protrusion can be found out, which is different from the asymmetric behavior on the macro-ridge. The deformation caused by the collision between the inner and outer rim generates a sharp increase in the curvature at the bottom of the liquid ring, which produces a sudden upward reaction force, leading to an earlier bouncing from the superhydrophobic surface.

### 1.1.2 Single and multiple triangular ridge

The droplet impacting a superhydrophobic surface equipped with macroscopic triangular ridges is simulated using the 3-D LBM and focus on the effects of  $We$  and the number of ridges on the dynamic behavior and contact time.

The change of  $We$  has great influence on the dynamic behavior when droplet impacting on single ridge. As  $We$  increases, the droplets gradually

switch from impacting to form a normal plane, forming a ring shape and splitting even further. The change of  $We$  has great influence on the contact time when droplet impacting on single ridge. When  $We$  is low, the contact time is basically constant around 1.5. However, with the increase of  $We$ , the contact time decreases sharply to around 1.0 due to the formation of ring. The ring causes the inner and outer edges of the droplet to contract toward the middle, and then generates an upward velocity, prompting the droplet to bounce up. As  $We$  continues to increase, the droplet splits during the impact, and the contact time of the droplet impact is further reduced to 0.84 (Figs.3(a,b)).

For the single ridge, as  $We$  increases, the droplet gradually forms a ring shape and the splits. The appearance of ring shape leads to a rapid decrease in contact time and  $We=11.47$  by about 50%—66.7%, which is because an opposite fluid movement in the inner and outer edges collides with each other and generates an upward velocity that facilitates the droplet bouncing. Based on the single ridge, the structure of cross ridges and quadruple ridges are proposed to research the effect of different number of ridges to the contact time.

The traditional way of dividing dynamic behavior divides the process of water droplets impacting an isosceles right triangular ridge into three stages: falling stage, spreading stage and retraction stage, as shown in Fig.3(c). However, we found this division to be inaccurate for the following reasons. Firstly, the spreading and retraction of the droplet on the ridge and the bottom substrate do not occur simultaneously, so a simple division of spreading and retraction hard to define the droplet behavior. Secondly, the droplet touches different surfaces at different stages and is subject to different surface forces, so spreading and retraction division is not reasonable. Therefore, in this paper, we divide the contact time into three stages based on the surface that the droplet touches: the descent stage, the bottom surface stage and the ascent stage.

Durations for three stages revealed that the main part of the decrease in contact time with in-

creasing  $We$  was the rapid decrease in ascent time, which is because of the larger asymmetry. Additionally, the crossed ridges structure (including cross

and quadruple ridges) helps to reduce the bottom surface time, which means it force the droplet to leave the bottom surface earlier (Figs.3(e, f)).

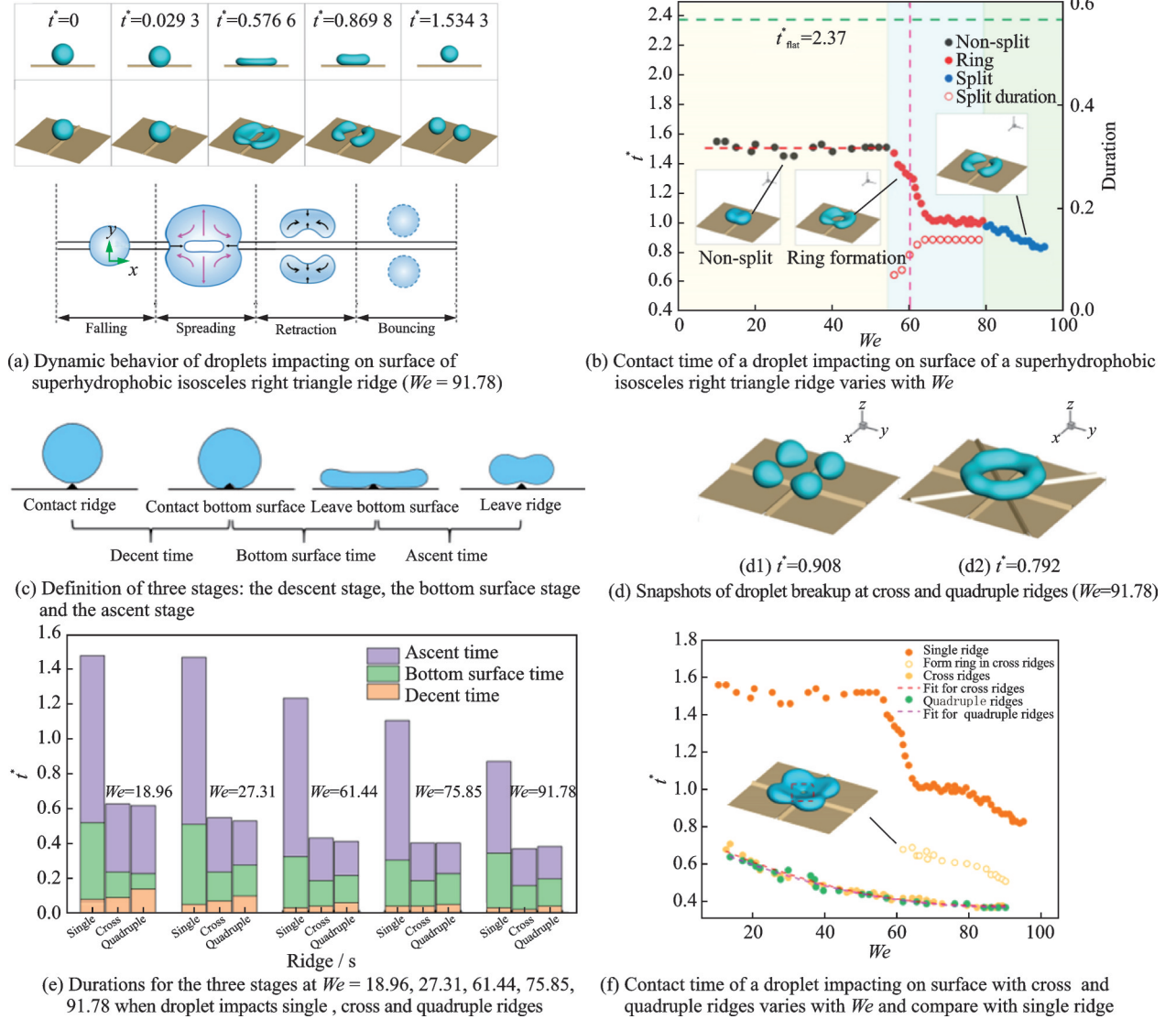


Fig.3 Dynamic behavior of a droplet impacting on superhydrophobic surface with triangular ridges

### 1. 1. 3 Suspended octagonal prism

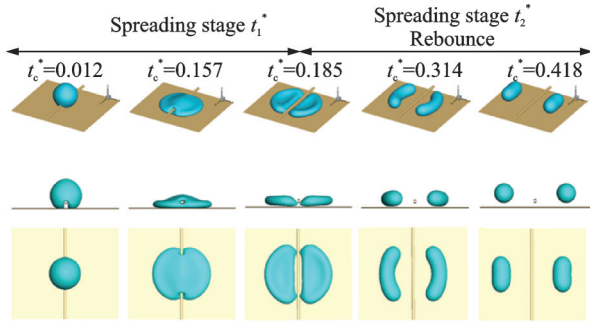
We study the droplet impacting dynamics on a superhydrophobic surface with a suspended octagonal prism by using LBM, and found that the asymmetric retraction of the impacting droplet strongly depends on the combined effect of  $We$  and the suspended height  $w$ .

The suspended prism destroys the axial symmetry during the spreading process and retracting process of droplet and effectively reduces the contact time. When the suspended height of the prism and the width of the prism are both fixed, the impact

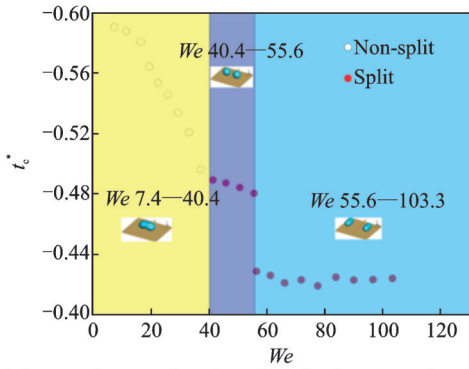
dynamics and the contact time variation show different trends with varying  $We$ . For  $We$  of 7.4—40.4, the droplet is not split and the contact time reduces continuously.  $We$  varies from 40.4 to 55.6, and the droplet is split into two sub-droplets, which results that contact time further reduces because the sub-droplets need to undergo a complete retraction process in the  $y$ -direction and  $x$ -direction, respectively, to leave the surface. When  $We$  exceeds 55.6, the contact time decreases sharply to 0.43 and remains almost unchanged because the sub-droplets only need to complete the retraction process in the  $y$ -di-

rejection to leave the surface. At the  $We$  of 55.6—103.3, the maximum reduction in contact time can reach about 59% compared to the superhydrophobic flat surface (Figs.4(a—c)).

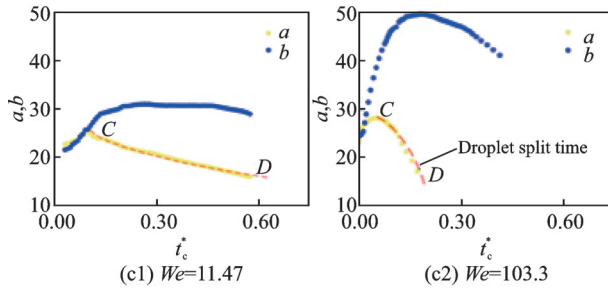
The suspended height of the prism shows great effect on the contact time. For  $We=11.47$ , when



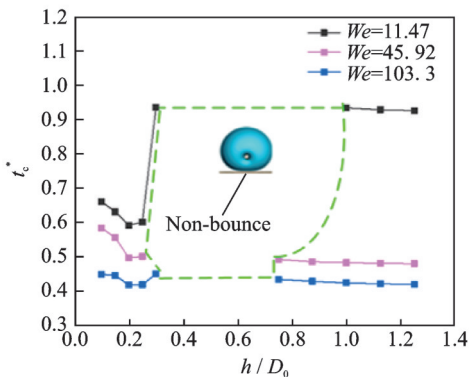
(a) Snapshots of the droplet impacting on the superhydrophobic surface with a suspended prism of  $w=4$ ,  $h/D_0=0.2$  at  $We=103.3$



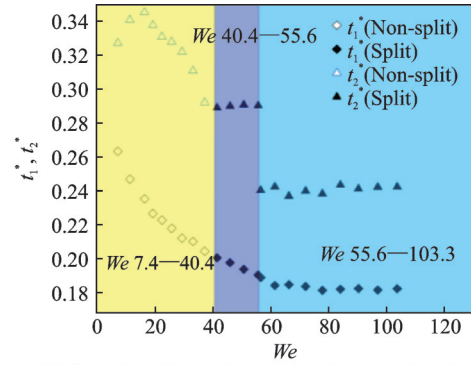
(b) Contact time as a function of  $We$  for the prism of  $w=4$ ,  $h/D_0=0.2$



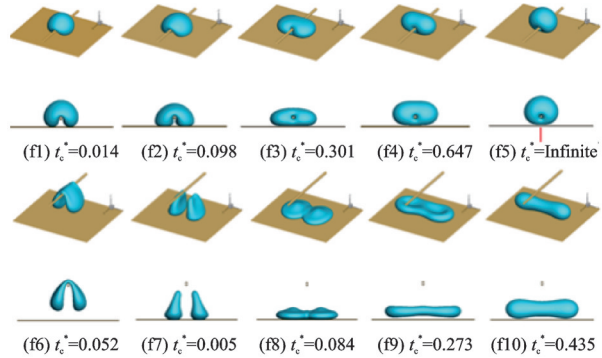
(c) Temporal variations of the axial direction expansion and the normal direction expansion for  $We=11.47$ , 103.3



(d) Contact time as a function of the suspended height of the prism at different  $We$



(e) Spreading time and retraction time as a function of  $We$



(f) Snapshots of droplet impacting on superhydrophobic surface with a suspended prism of  $w=4$ ,  $h/D_0=0.35$ , and  $w=4$ ,  $h/D_0=1$  at  $We=11.47$

Fig.4 Dynamic behavior of a droplet impacting on superhydrophobic surface with a suspended prism

the ratio of prism height to the droplet diameter  $h/D_0$  is in the range of 0.1—0.3, the droplet is not split, and the contact time first reduces and then increases distinctly. At  $We=45.92$ , the droplet is split only when  $h/D_0$  is larger than 0.15, but can be split for any suspended height at  $We=103.3$ . For  $We=103.3$ , when  $h/D_0=0.2$ , each split film only needs to retract along the  $y$ -direction before leaving the surface, which leads to reduction in the contact time. When  $h/D_0$  is larger than 0.75 at  $We=103.3$ , the impact dynamics differ from that at  $We=11.47$ . The droplet is split into two sub-droplets before contacting the surface and then undergoes the process of coalescence, retraction in the  $x$ -direction to leave the surface, which leads to reduced contact time. Therefore, for  $We=103.3$ ,  $h/D_0=0.2$ , or larger than 0.75 is the most beneficial for reducing the contact time.

For  $We=11.47$  and 103.3, when  $h/D_0$  exceeds  $\sim 0.3$ , the droplet cannot bounce off the surface, but it cannot bounce off the surface as  $h/D_0$  exceeds  $\sim 0.25$  for  $We=45.92$ . This is mainly be-

cause the film beneath the prism always wraps the prism and cannot be split by the prism, which causes the droplet fails to rebound from the surface. The velocity field demonstrates that the droplet upward velocity is offset by the prism, and the attenuation in transverse velocity hinders the breakup of the liquid bridge under the prism.

## 1.2 Droplet impacting on the tilted cold surface

Droplet impacting on a tilted and cold substrate involves both droplet unidirectional motion and phase change process, which is more complex droplet impacting on a flat surface. Up to now, the research on the droplet dynamics and phase change evolution under the coupled influence of inclination angle and cold surface temperature is not refined enough. The freezing mode of droplets after impacting inclined cold surfaces is not clear yet.

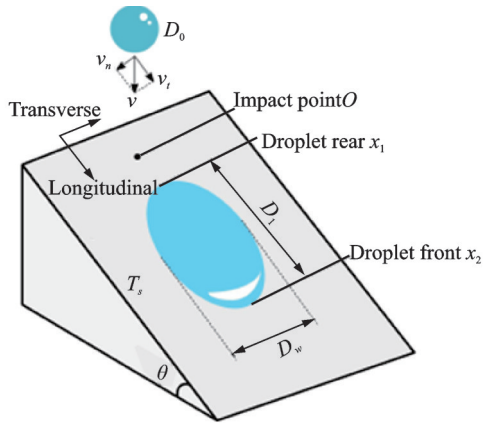
We carried out a visualization study on the behavior of droplets impacting inclined cold surfaces, after a droplet impacts a tilted cold surface, it will quickly spread, causing the rear liquid film to be thinner. When the surface temperature is low enough, the rear liquid film close to the cold surface freezes first, forming a frozen layer, as shown in Figs.5(a, c). At this time, because the front liquid on the upper layer has not frozen, its surface tension further overcomes gravity and shear stress between the liquid layers and flows back to the rear of the droplet. Due to the decrease in temperature, kinetic energy dissipates rapidly. The backflow liquid film freezes before reaching the interface between the frozen liquid film and the cold surface, forming a secondary freezing layer. After multiple oscillations and backflows, tertiary freezing layers and quaternary freezing layers can be successively superimposed until the droplet is completely frozen.

Fig.5(b) shows the distribution of the droplet freezing mode after the droplet hits the inclined cold surface. It can be seen from the figure that under the combined effect of the cold surface temperature  $T_s$  and the inclination angle  $\theta$ , the shapes of droplet impact freezing can be divided into: circular pie freezing, elliptical pie freezing, ellipsoid retraction freez-

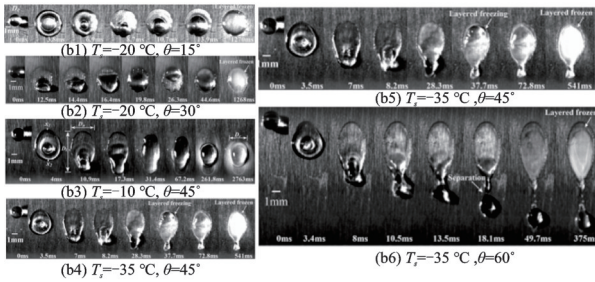
ing, and single liquid finger freezing and the single liquid refers to broken freezing, as shown in Fig.5(d). It can be seen from the figure that when the temperature of the cold surface is high and the inclination angle is large, the droplet is prone to retraction due to the late freezing time, and finally presents an ellipsoidal frozen morphology. When the inclination angle is small ( $15^\circ$ ), the influence of the inclination angle is small, and the droplets freeze in the shape of a round cake. When the inclination angle is further increased to  $30^\circ$ , due to the effect of gravity, the droplets will be stretched in the longitudinal direction, forming an elliptical pie-shaped freeze. When the inclination angle is further increased, reaching  $45^\circ$ , the droplets begin to appear fingers and freeze rapidly. When the inclination angle reaches  $60^\circ$  and the cold surface temperature reaches  $-35^\circ\text{C}$ , the liquid finger breaks, presenting a pattern of liquid finger breaking and freezing.

Fig.5(e) shows the variation of the droplet freezing time with the inclination angle and the temperature of the cold surface. It should be pointed out that the freezing time here refers to the freezing time of the primary droplet, excluding the freezing of the secondary droplet. It can be seen from the figure that with the increase of the inclination angle of the wall, the freezing time of the droplet tends to decrease. This is because the increase of the inclination angle promotes the increase of the longitudinal spread of the droplet, but the change of the lateral spread is small, making the overall spread of the droplet. As the area increases, the heat transfer effect is enhanced. In addition, the rapid spreading makes the liquid film of the back-end droplets thinner and the freezing time is shortened. In addition, it can also be seen from the figure that the freezing time of 2.5 mm droplets is less than 1.5 s when the cold surface temperature is lower than  $-20^\circ\text{C}$ . When the inclination angle  $\theta > 45^\circ$ , the droplet freezing time is less than 1 s. When the cold surface temperature is  $-35^\circ\text{C}$  and the inclination angle is  $60^\circ$ , it only takes 375 ms for the main droplet to completely freeze. It can be seen from the above that the large inclination angle combined with the

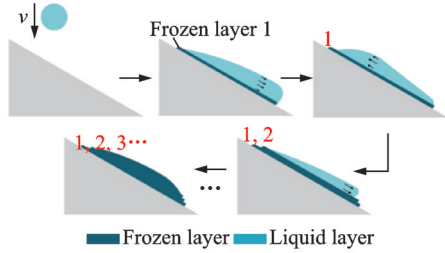
low cold surface temperature can significantly reduce the droplet freezing time.



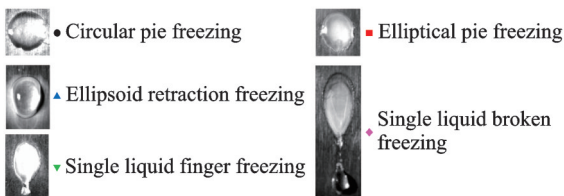
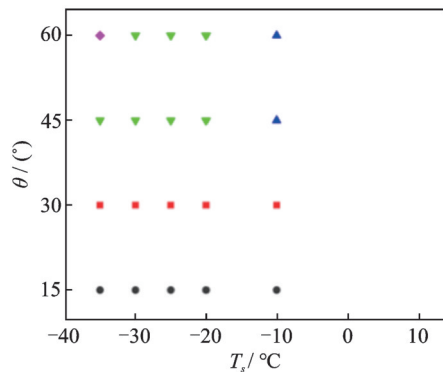
(a) Diagram of droplet impact on tilted cold surface



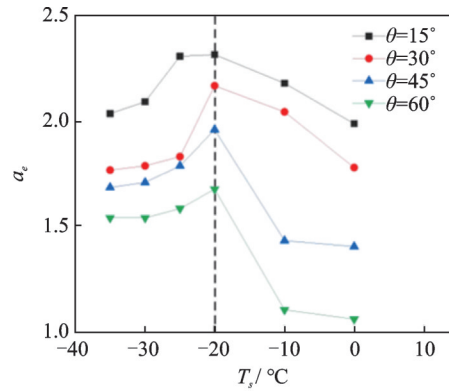
(b) Evolution of droplet impacting on inclined cold surface with different substrate surface temperatures  $T_s$  and inclined angles  $\theta$



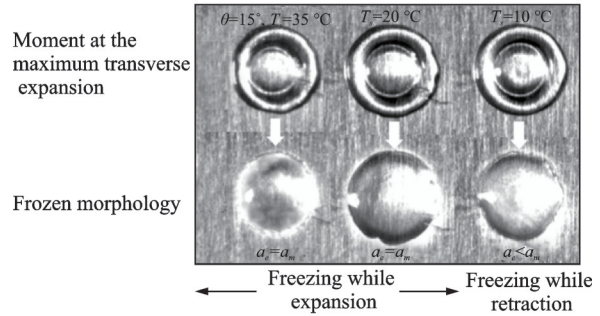
(c) Schematic diagram of layered freezing process



(d) Different freezing mode distribution as a function of substrate surface temperature



(e1) Droplet freezing transverse spreading factor variation with  $T_s$  and inclination angle



(e2) Comparison of droplet transverse spreading factor  $a_e$  to droplet freezing diameter  $a_m$

(e) Variation of droplet freezing transverse final spreading factor  $a_e$  with substrate surface temperature

Fig.5 Freezing dynamics of a droplet impacting on a tilted surface

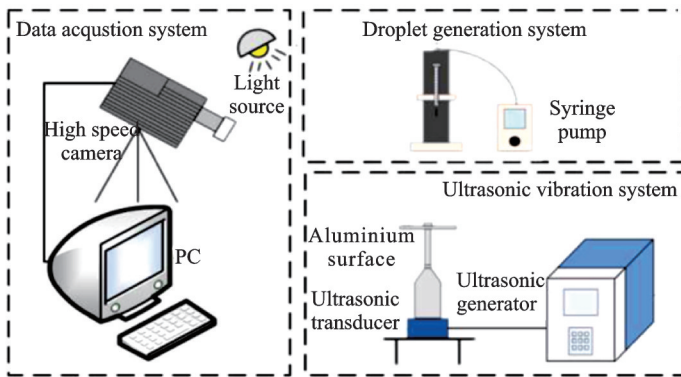
### 1.3 Droplet impacting dynamics on ultrasonic vibrated surface

The dynamics of a droplet impacting on an ultrasonic vibrated circle surface was experimentally studied, and the experiment setup is given in Fig.6(a). The results demonstrated that four typical impact dynamic modes, including the surface uniform atomization, the unilateral directional spreading atomization, the split atomization on both sides, and the sub-balance state, were observed.

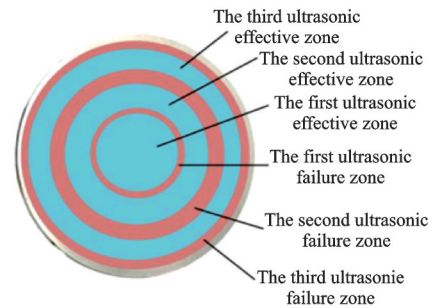
The distribution of the shear force that induced by the ultrasonic vibration was not linearly decrease along radial direction out (Fig.6(b)). The ultrasonic effective zone and failure zone can be seen alternately on the circular surface and the droplet cannot effectively be removed, if it hits the ultrasonic failure zone, even though the impact point is close to the vibration source. The uneven forces induced by the ultrasonic vibration resulted in four typical impact dynamics modes as the droplet impacting on the ultrasonic vibrated surface: Surface uniform at-

omization, unilateral directional spreading atomization, split atomization on both sides, and sub-balance state, which is related to the impact position (Fig.6(c)). In the ultrasonic effective area, surface uniform atomization and unilateral directional spreading atomization are more likely to occur. As shown, the droplet first quickly spreads as it impacts on the surface and the capillary wave can be clearly observed on the droplet surface due to ultrasonic vibration. With the droplet spreading to a thinner liquid film, the surface capillary wave can be sig-

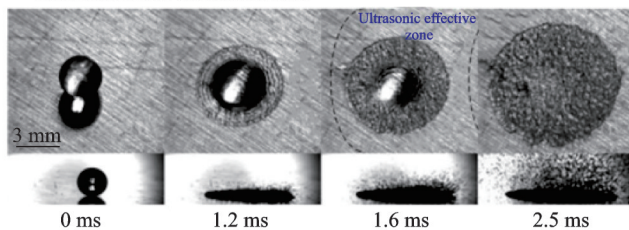
nificantly enhanced, leading to a great number of tiny droplets eject from the both sides of the droplet surface, which can promote the droplets atomization and removal. At 4.75 ms, the droplet spreading process reaches to the maximum and the retraction occurs. The liquid film on both sides can gradually shrink inward until the whole atomization process ends, which is completely different from that on the surface without ultrasonic vibration. It should be noted that at the end of the impacting, almost no droplet can be seen on the surface and the droplet can be



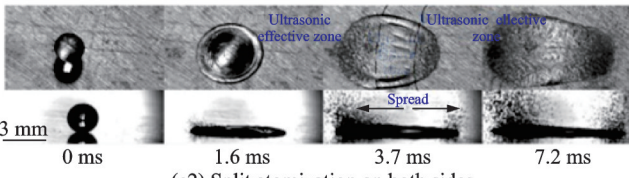
(a) Schematic diagram of the experimental setup concerning droplet impacting on an ultrasonic vibrated surface



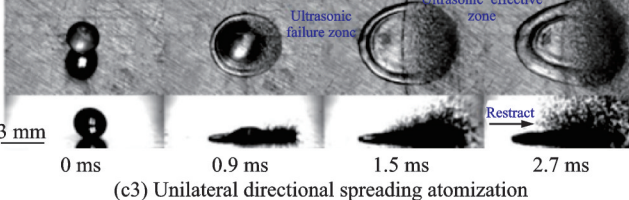
(b) Division of the ultrasonic effective zones and failure zones



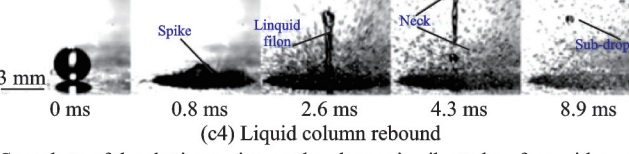
(c1) Surface uniform atomization



(c2) Split atomization on both sides

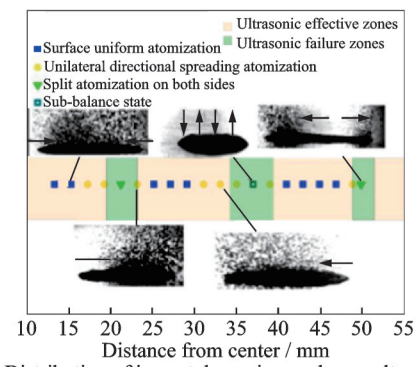


(c3) Unilateral directional spreading atomization

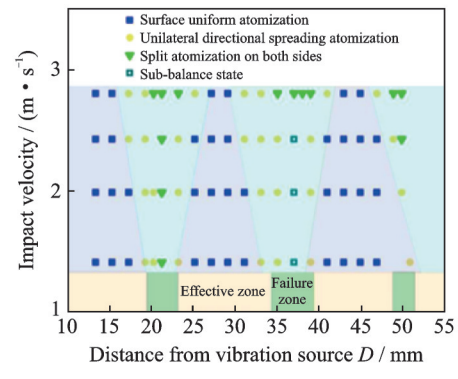


(c4) Liquid column rebound

(c) Snapshots of droplet impacting on the ultrasonic vibrated surface with surface uniform atomization, unilateral directional spreading atomization, split atomization and liquid column rebound



(d) Distribution of impact dynamics modes on ultrasonic vibrated circular surface



(e) Impact dynamics modes under various impact velocities

Fig.6 Impacting droplet atomization induced by ultrasonic vibration

effectively removed in 1 s. During the uniform atomization, a unique liquid column rebound phenomenon is observed. During the droplet spreading process, the centered liquid spreading is suppressed with a spike, which further evolves into a cylindrical slender column and eject from the surface. If droplet impacts on the ultrasonic failure area, the split atomization, unilateral directional spreading atomization, and sub-balance state can be observed. Unilateral directional spreading atomization at the impacting point B located at the boundary between the ultrasonic failure and effective zones. At 1.5 ms, the right liquid film spreading into the atomization effective zone can be violently atomized and a large number of micro-droplets released from the droplet surface. Split atomization on both sides, can be seen in Fig.6(c) when the droplet impacts on the point *D* at the ultrasonic failure zone. Both the left and right sides rapidly spread and finally get into the ultrasonic effective zone, which induce both side atomization, but with droplet central stably unmoved. As the droplet impacts on the ultrasonic failure zone, the droplet first rapidly spreads outward but the whole droplet still in the ultrasonic failure zone. The droplet then retracts with a long-time self-oscillation, and no atomization is observed.

Fig.6(d) presents the impact dynamic mode distributions on the circular surface excited by the ultrasonic vibration with input power 18 W and impact velocity 1.98 m/s. The droplet impact dynamics and atomization modes are related to the impact position. Based on the experimental result, four ultrasonic effective zones and three failure zones could alternately appear on the circular surface. Here, the yellow and green blocks represent the ultrasonic effective zone and failure zone, respectively. In the ultrasonic effective area, surface uniform atomization and unilateral directional spreading atomization are more likely to occur. If droplet impacts on the ultrasonic failure area, the split atomization, unilateral directional spreading atomization, and sub-balance state can be seen. The unilateral directional spreading atomization can happen in the ultrasonic effective and failure zones if only the impact point is close to the boundary of the two zones.

Fig.6(e) shows the impact dynamics modes distribution under various impact velocities. As the impact velocity is just 1.4 m/s, fully spreading of the droplet cannot cross two zones, the uniform atomization tends to appear in the ultrasonic effective zone, and the sub-balance can be seen in the ultrasonic failure zone. However, with the impact velocity increasing up to 2.8 m/s, some of the uniform atomization will turn into the unilateral directional spreading atomization on the same impacting position. The ultrasonic vibration could promote the spreading of the droplet, and the effects of different impact dynamics modes on the spreading factor are totally different. Therein, the spreading factor can reach to the maximum in the split impact dynamic mode. In addition, the impact dynamics modes can be changed by the impact velocity.

## 2 De-icing

### 2.1 Freezing droplet removal by the ultrasonic vibration

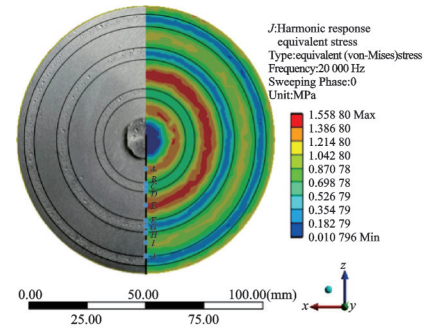
An experimental study concerning the removal of iced droplets from cold flat surface by ultrasonic vibration was conducted. The detailed dynamic behavior of iced droplets located on different position of the cold surface subjected to 20 kHz ultrasonic vibration was observed. The ultrasonic vibration results in a ring-shape uneven equivalent stress distribution, which led to different residual characteristics of the iced droplets in different zones. It is found that the iced droplets adhered on the cold surface can be removed instantaneously by the ultrasonic vibration. From both experiments and frequency domain simulation, we demonstrated that, on the circular plate, the distribution of equivalent stress induced by the ultrasonic vibration corresponded to the alternately appeared deicing effective and failure zones. The counterintuitive results not only revealed the reason why the deicing performance does not depend on the radial distance, but also specified the role of equivalent stress on deicing. According to the division of deicing effective and failure zone, different ice residual characteristics were observed. Four typical residual states can be seen on the sur-

face after ultrasonic vibration, which were crescent residue, stripe residue, no residue and complete residue.

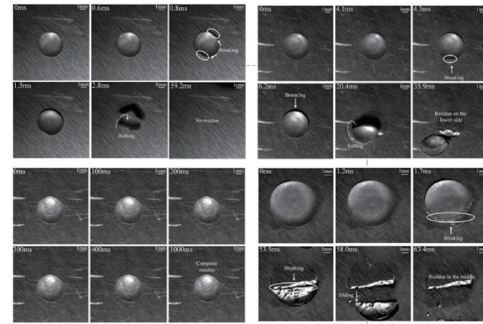
Figs.7(a, b) show the complete removal of the iced droplet in the ultrasonic effective zone. The first 0.6 ms after onset of the ultrasound generator was an accumulating energy process. At 0.8 ms, the upper and lower sides of the ice droplet broke up due to the strong equivalent stress in the two regions. With continuous ultrasonic excitation, the iced droplet completely departed from the surface at 1.5 ms, and the iced droplet bounced off from the substrate. Unilateral removal of iced droplet was found at the boundary between the ultrasonic failure zone and effective zone. After 1 s of ultrasonic excitation, most of the droplets had been removed and some ice crystals on the lower side left, which was in the weak equivalent stress zone. The iced droplet removal failure can be found in the weak equivalent stress zone. After 1 s ultrasonic excitation, the iced droplet could not break, bounce or rotate. The droplet stretched over two strong equivalent stress zone could present a bilateral removal. The upper and lower sides of the iced droplet subsequently removed from the surface, and the ice crystals in the middle resided after ultrasonic vibration. Fig.7(c) depicts the residual ice distribution on circular plate under ultrasonic vibration. The de-icing effective and failure zones could be divided according to the distribution of equivalent stress. As shown, the ice residue was in the regions where the equivalent stress was relatively weak and the ice residual states were related to equivalent stress distribution. In contrast, the iced droplet could be completely removed on the interface and no residue could be seen in the strong equivalent stress area.

The iced droplet removal time and surface temperature in different positions of the surface were different due to the uneven distribution of equivalent stress on the surface. The removal time of the iced droplet located on the surface with greater equivalent stress can be shortened. To further explore the effect of uneven distribution of equivalent stress caused by ultrasonic vibration, the variation of surface temperature with time was recorded in different

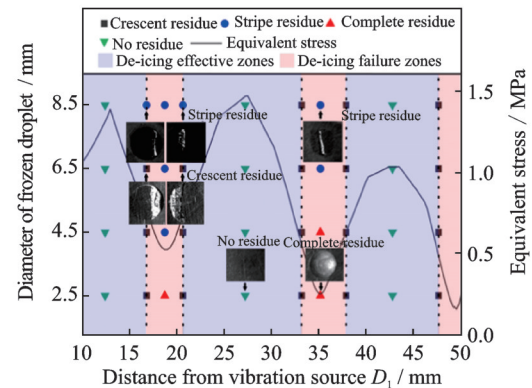
locations, as shown in Figs.7(d, e). A sharply temperature rising could be seen after ultrasonic vibration, which was attributed to the friction effects caused by ultrasonic vibration. Subsequently, the temperature decreasing occurred after the 1 s ultrasonic excitation. The maximum temperature rise



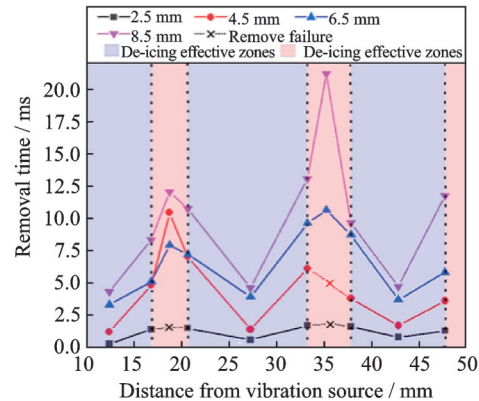
(a) Equivalent stress distribution of circular surface excited by 20 kHz ultrasound



(b) Dynamic behavior of iced droplet removal: complete removal, unilateral removal, removal failure and bilateral removal



(c) Residual states distribution of iced droplets under ultrasonic vibration



(d) Removal time of iced droplets under ultrasonic vibration

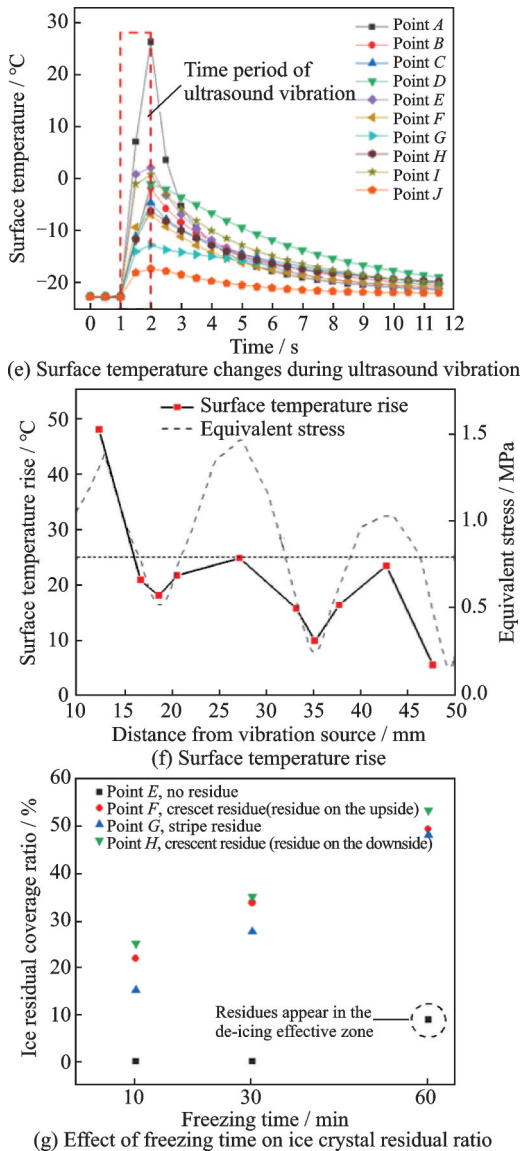


Fig.7 Freezing droplet removal by ultrasonic vibration

was  $24.8\text{ }^{\circ}\text{C}$ . Although a significant surface temperature rising could be observed during the ultrasonic vibration, the thermal effect on the de-icing was limited. Due to the short action time of ultrasonic vibration, the heat transferred to the ice was minute.

The freezing time of the iced droplet also affected the droplet removal by ultrasonic vibration. As shown in Figs.7(f, g), for iced droplets in the freezing time from 10 min to 60 min and ambient temperature from  $-15\text{ }^{\circ}\text{C}$  to  $-35\text{ }^{\circ}\text{C}$ , the ice residual coverage ratio gradually increased with the ultrasonic input power 18 W.

## 2.2 Frost removal by the ultrasonic wave

Different from single ice droplet, the frost a frost is a cover of tiny ice crystals on freezing-cold

objects exposed to the air. Researchers at home and abroad have carried out a lot of research on the defrosting, such as thermal defrosting, surface wettability, and electric field frost suppression. Thermal defrosting has the advantages of fast defrosting and thorough defrosting, but at the end of defrosting, a large number of defrosting droplets will be produced, which will become the base of secondary frosting. The ultrasonic vibration, with its advantages of high efficiency and energy saving, attract much interest in the field of surface defrosting. The results showed that ultrasonic waves can effectively remove frost at the initial stage of frosting, but is less effect in removing dense frost layers. The selection of ultrasonic frequency should be adjusted according to the resonance frequency of the frost lay and system. In our work, we used the high-speed camera to observe the dynamic behavior of the frost layer on the vertical cold surface under the action of ultrasound. The experimental results were compared with the shear force analysis, and finally revealed the effects of ultrasonic action time and frosting time on defrosting efficiency.

Fig.8(a) shows the dynamic behavior of frost shedding at the moment of ultrasonic vibration. The substrate temperature is  $-10\text{ }^{\circ}\text{C}$ . At the moment of ultrasonic action, small frost crystals around the central ultrasonic vibration source and at the edge of the plate broke from the top of the frost layer and detached from the plate. At 73 ms, the frost layer began to bulge, showing bilateral symmetry. At 85 ms, the uplift of the left and right frost layers became more obvious, and the frost layer began to break and fall off. At 97 ms, the cracked frost layer peeled off from the cold surface and bounced off from the vertical cold surface. By 297 ms, the apparent frost layer had completely fallen off except for a relatively dense frost base layer. The uneven removal of frost lay depended on the non-uniform distribution of equivalent stress caused by the ultrasonic wave. At the moment of ultrasonic action, the frost layer bulge in the area with higher equivalent stress, and the frost layer is easier to peel off. The frost layer in the area with lower stress is barely removed, as shown in Figs.8(b, c).

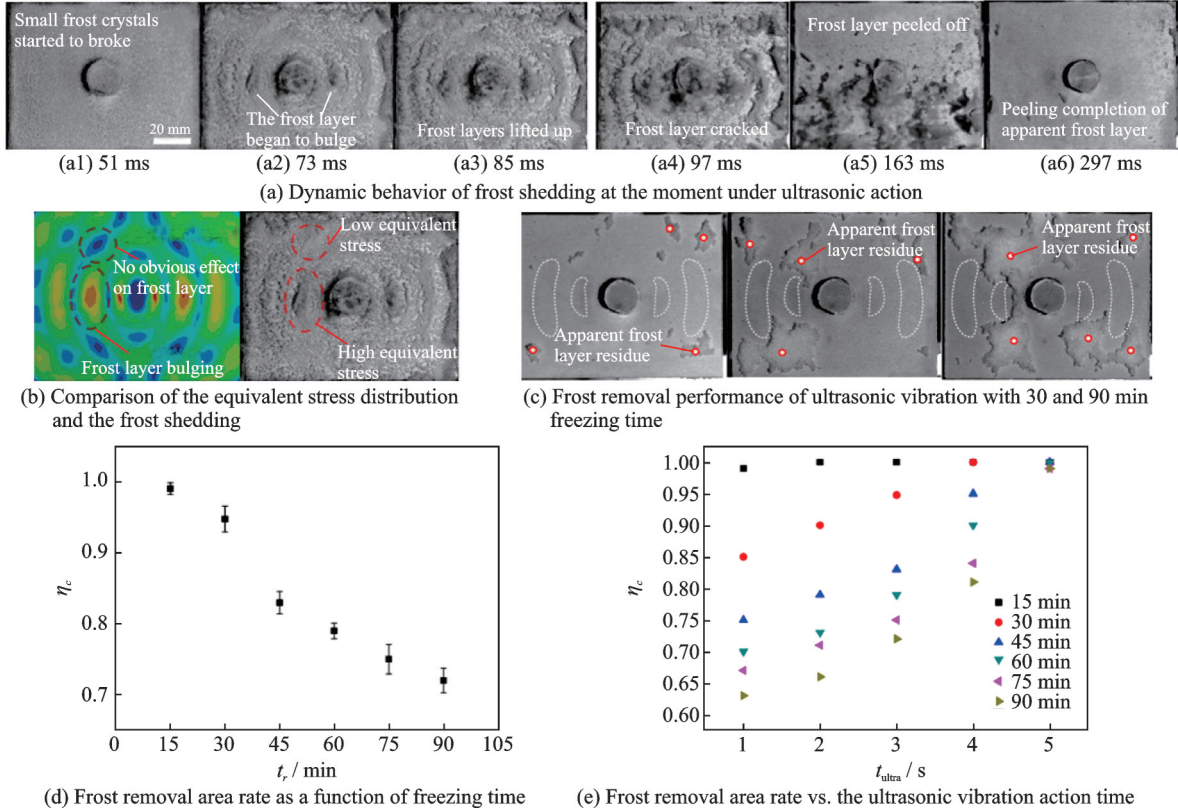


Fig.8 Frost shedding by ultrasonic vibration

The surface frost area removal rate (the ratio of the surface area of the frost layer removed by ultrasonic to the area of the flat plate) was quantitatively analyzed at different frosting times, as shown in Fig.8(d). It can be seen from that when the frosting time is 15 min, the frost layer above the substrate can be almost completely removed. When the frosting time is more than 30 min, the ultrasonic excitation cannot completely overcome the adhesion between the frost layer and the cold surface, and completely remove the frost layer on the substrate. And with the increase of frosting time, the removal rate of frost layer further decreased. When the frosting time was 90 min, the removal rate of frost layer dropped to about 70%.

Fig.8(e) shows that the removal rate of the frost layer increases with the growing of ultrasonic action time. When the ultrasonic action time is less than 3 s, except for the case where the frosting time is 15 min, there leaves a residual frost layer. When the ultrasonic action time is increased to 5 s, the frost layer on the cold surface can nearly be removed. This is because the increase of ultrasonic ac-

tion time can generate continuing shear force, which further overcomes the adhesion between the frost layer and the surface. On the other hand, the ultrasonic thermal effect melts the base of the frost layer and reducing the adhesion of the interface.

### 3 Conclusions

The dynamic behavior of droplets impacting on the substrate and ultrasonic vibration assistant droplet manipulation involve complex mass and heat transfer. We conducted numerical simulations and experiments intent to explain the underlying physics and to optimize surface morphology and the ultrasonic input parameters to enhance its ability in anti-icing and de-icing. Here, we conclude as follows:

(1) The macro-structure decorated superhydrophobic surface exhibit remarkable capability in contact time reduction. The macro-structures, varying from 0-dimensional cubic protrusion, to 1-D triangular ridge, to 2-D crossed ridges and finally to 3-D suspended prism, can control the droplet deformation in both expansion and retraction process. The unusual deformation leads to complex droplet inter-

nal flow and thus change the expansion and retraction process. The contact time variation with  $We$  show a steep drop when reaching a certain number, where the droplet shows obvious deformation due to the macro-structure. Through the numerical simulation, we revealed that the heterogeneous deformation is the main reason for fast droplet bouncing.

(2) The dynamics and freezing behavior of droplet impacting the tilted cold surface was investigated. When droplet hits the tilted cold surface, there appears layered backflow and pulse oscillation, which makes the droplet's layered freezing. The larger inclination angle and lower surface temperature result in more obvious layered freezing phenomenon and thus different droplet freezing modes. With the decrease in surface temperature, the transverse final state expansion factor reaches maximum at the critical temperature  $-20\text{ }^{\circ}\text{C}$ , which is regardless of the inclination angle.

(3) The ultrasonic vibration is demonstrated facilitative in both anti-icing and de-icing processes. For droplet impacting on an ultrasonic vibrated surface, the impact dynamic modes are determined by the uneven distribution of the equivalent shear stress caused by the ultrasonic wave. The different droplet impact modes divide the substrate into ultrasonic effective zone and failure zone, which is not appeared as radial linear distribution but as an alternating form. Therefore, the droplet impacting at different places shows different atomization modes, such as uniform atomization, the unilateral directional spreading atomization, the split atomization and the non-atomized sub-balance state.

(4) The effective of ultrasonic vibration in de-icing was experimentally studied for both single droplet and frost. On the ultrasonic effective and failure zone, the removal performance of the iced droplet and frost are both corresponding to the equivalent shear stress distribution. For single droplet the residue after ultrasonic vibrating presents different shapes at different positions.

The processing involving droplet dynamics and phase change is critical in enhancing the anti-icing and de-icing performance. Our research outcomes can provide several parallel potential ways of im-

proving the anti-icing and de-icing efficiency. The combination of passive and active anti-icing and de-icing methods can be a promising approach.

## References

- [1] VOLPE A, GAUDIUSO C, ANCONA A. Laser fabrication of anti-icing surfaces: A review[J]. *Materials*, 2020, 13(24): 5692.
- [2] PELLISSIER M, HABASHI W, PUEYO A. Optimization via FENSAP-ICE of aircraft hot-air anti-icing systems[J]. *Journal of Aircraft*, 2011, 48 (1) : 265-276.
- [3] SU Qian, CHANG Shinan, SONG Mengjie, et al. An experimental study on the heat transfer performance of a loop heat pipe system with ethanol-water mixture as working fluid for aircraft anti-icing[J]. *International Journal of Heat and Mass Transfer*, 2019, 139: 280-292.
- [4] LIN Yuebin, CHEN Haifeng, WANG Guanyu, et al. Recent progress in preparation and anti-icing applications of superhydrophobic coatings[J]. *Coatings*, 2018, 8(6): 208.
- [5] RUAN Min, LI Wen, WANG Baoshan, et al. Preparation and anti-icing behavior of superhydrophobic surfaces on aluminum alloy substrates[J]. *Langmuir*, 2013, 29(27): 8482-8491.
- [6] LYU Jianyong, SONG Yanlin, JIANG Lei, et al. Bio-inspired strategies for anti-icing[J]. *ACS Nano*, 2014, 8(4): 3152-3169.
- [7] GOLOVIN K, KOBAKU S P, LEE H, et al. Designing durable icephobic surfaces[J]. *Science Advances*, 2016, 2(3): e1501496.
- [8] SHEN Yizhou, WU Xinghua, TAO Jie, et al. Icephobic materials: Fundamentals, performance evaluation, and applications[J]. *Progress in Materials Science*, 2019, 103: 509-557.
- [9] ZHANG Hongqiang, ZHAO Guanlei, WU Shuwang, et al. Solar anti-icing surface with enhanced condensate self-removing at extreme environmental conditions[J]. *Proceedings of the National Academy of Sciences*, 2021, 118(18): e2100978118.
- [10] ZHOU Xiaoteng, SUN Yuling, LIU Jie. Designing anti-icing surfaces by controlling ice formation[J]. *Advanced Materials Interfaces*, 2021, 8(17): 2100327.
- [11] LIU Bo, ZHANG Kaiqiang, TAO Chao, et al. Strategies for anti-icing: Low surface energy or liquid-infused[J]. *RSC Advances*, 2016, 6(74): 70251-70260.
- [12] WANG Feng, ZHUO Yizhi, HE Zhiwei, et al. Dynamic anti-icing surfaces (DAIS)[J]. *Advanced Science*, 2021, 8(21): 2101163.

- [13] KREDER M J, AJVARENGA J, KIM P, et al. Design of anti-icing surfaces: Smooth, textured or slippery[J]. *Nature Reviews Materials*, 2016, 1(1): 1-15.
- [14] ZHANG Songnan, HUANG Jianying, CHENG Yan, et al. Bioinspired surfaces with superwettability for anti-icing and ice-phobic application: Concept, mechanism, and design[J]. *Small*, 2017, 13(48): 1701867.
- [15] DOU Renmei, CHEN Jing, ZHANG Yifan, et al. Anti-icing coating with an aqueous lubricating layer [J]. *ACS Applied Materials & Interfaces*, 2014, 6(10): 6998-7003.
- [16] GUO Chunfang, ZHAO Danyang, SUN Yanjun, et al. Droplet impact on anisotropic superhydrophobic surfaces[J]. *Langmuir*, 2018, 34(11): 3533-3540.
- [17] SCHUTZIUS T M, JUNG S, MAITRA T, et al. Spontaneous droplet trampolining on rigid superhydrophobic surfaces[J]. *Nature*, 2015, 527(7576): 82-85.
- [18] BIRD J C, DHIMAN R, KWON H M, et al. Reducing the contact time of a bouncing drop[J]. *Nature*, 2013, 503(7476): 385-388.
- [19] GAUTHIER A, SYMON S, CLANET C, et al. Water impacting on superhydrophobic macrotextures[J]. *Nature Communications*, 2015, 6: 8001.
- [20] SHEN Y, TAO J, TAO H, et al. Approaching the theoretical contact time of a bouncing droplet on the rational macrostructured superhydrophobic surfaces[J]. *Applied Physics Letters*, 2015, 107(11): 111604.
- [21] REGULAGADDA K, BAKSHI S, DAS S K. Triggering of flow asymmetry by anisotropic deflection of lamella during the impact of a drop onto superhydrophobic surfaces[J]. *Physics of Fluids*, 2018, 30(7): 072105.
- [22] HU Zhifeng, WU Xiaomin, CHU Fuqiang, et al. Off-centered droplet impact on single-ridge superhydrophobic surfaces[J]. *Experimental Thermal and Fluid Science*, 2021, 120: 110245.
- [23] ABOLGHASEMIBIZAKI M, MOHAMMADI R. Droplet impact on superhydrophobic surfaces fully decorated with cylindrical macrotextures[J]. *Journal of Colloid and Interface Science*, 2018, 509: 422-431.
- [24] HAO Pengfei, LV Cunjing, NIU Fenglei, et al. Water droplet impact on superhydrophobic surfaces with microstructures and hierarchical roughness[J]. *Science China Physics, Mechanics & Astronomy*, 2014, 57: 1376-1381.
- [25] SONG Meirong, LIU Zhaohui, MA Yongjian, et al. Reducing the contact time using macro anisotropic superhydrophobic surfaces—Effect of parallel wire spacing on the drop impact[J]. *NPG Asia Materials*, 2017, 9(8): e415-e415.
- [26] LIU Yahua, ANDREW M, LI Jing, et al. Symmetry breaking in drop bouncing on curved surfaces[J]. *Nature Communications*, 2015, 6(1): 10034.
- [27] ANDREW M, LIU Yahua, YEOMANS J M. Variation of the contact time of droplets bouncing on cylindrical ridges with ridge size[J]. *Langmuir*, 2017, 33(30): 7583-7587.
- [28] CHANTELOT P, MOQADDAM A M, GAUTHIER A, et al. Water ring-bouncing on repellent singularities[J]. *Soft Matter*, 2018, 14(12): 2227-2233.
- [29] LIN Dianji, WANG Liang, WANG Xiaodong, et al., Reduction in the contact time of impacting droplets by decorating a rectangular ridge on superhydrophobic surfaces[J]. *International Journal of Heat and Mass Transfer*, 2019, 132: 1105-1115.
- [30] LIN Dianji, ZHANG Lingzhe, YI Mengchao, et al. Contact time of double-droplet impacting superhydrophobic surfaces with different macrotextures[J]. *Processes*, 2020, 8(8): 896.
- [31] LIU Chunbao, LIU Qi, LIN Zhaohua. Dynamical behavior of droplets transiently impacting on superhydrophobic microstructures[J]. *Physics of Fluids*, 2020, 32(10): 103304.
- [32] ZHANG Yundian, HAN Longshen. Design and simulation of a kind of ultrasonic deicing acoustic system [J]. *Applied Mechanics and Materials*, 2012, 203: 500-503.
- [33] DANILIUOK V, XU Yuanming, LIU Ruobing, et al. Ultrasonic de-icing of wind turbine blades: Performance comparison of perspective transducers[J]. *Renewable Energy*, 2020, 145: 2005-2018.
- [34] LI Dong, CHEN Zhenqian. Experimental study on instantaneously shedding frozen water droplets from cold vertical surface by ultrasonic vibration[J]. *Experimental Thermal and Fluid Science*, 2014, 53: 17-25.
- [35] SHI Zhonghua, KANG Zhenhang, XIE Qiang, et al. Ultrasonic deicing efficiency prediction and validation for a flat deicing system[J]. *Applied Sciences*, 2020, 10(19): 6640.
- [36] WANG Zhenjun. Recent progress on ultrasonic de-icing technique used for wind power generation, high-voltage transmission line and aircraft[J]. *Energy and Buildings*, 2017, 140: 42-49.
- [37] ZHANG Leigang, SHI Juan, XU Bo, et al. Experimental study on distribution characteristics of condensate droplets under ultrasonic vibration[J]. *Microgravity Science and Technology*, 2018, 30: 737-746.

- [38] ZHANG Haixiang, ZHANG Xiwen, YI Xian, et al. Dynamic behaviors of droplets impacting on ultrasonically vibrating surfaces[J]. *Experimental Thermal and Fluid Science*, 2020, 112: 110019.
- [39] DEEPU P, PENG C, MOGHADDAM S. Dynamics of ultrasonic atomization of droplets[J]. *Experimental Thermal and Fluid Science*, 2018, 92: 243-247.
- [40] VUKASINOVIC B, SMITH M K, GLEZER A. Mechanisms of free-surface breakup in vibration-induced liquid atomization[J]. *Physics of Fluids*, 2007, 19(1): 012104.
- [41] SONG Yulin, CHENG C H, REDDY M K, et al. Simulation of onset of the capillary surface wave in the ultrasonic atomizer[J]. *Micromachines*, 2021, 12(10): 1146.
- [42] LIU Fushui, KANG Ning, LI Yikai, et al. Experimental investigation on the atomization of a spherical droplet induced by Faraday instability[J]. *Experimental Thermal and Fluid Science*, 2019, 100: 311-318.
- [43] WANG Yunda, ZHANG Gang, TIAN Zhongbei, et al. An online thermal deicing method for urban rail transit catenary[J]. *IEEE Transactions on Transportation Electrification*, 2020, 7(2): 870-882.
- [44] WANG Zhenjun, XU Yuanming, SU Fei, et al. A light lithium niobate transducer for the ultrasonic de-icing of wind turbine blades[J]. *Renewable Energy*, 2016, 99: 1299-1305.
- [45] WANG Y, Y XU, LEI Y. An effect assessment and prediction method of ultrasonic de-icing for composite wind turbine blades[J]. *Renewable Energy*, 2018, 118: 1015-1023.
- [46] PALACIOS J L, SMITH E C, ROSE J L. Investigation of an ultrasonic ice protection system for helicopter rotor blades[C]//Proceedings of the American Helicopter Society 64th Annual Forum. Montreal, Canada: AHS, 2008.
- [47] PALACIOS J L, SMITH E C. Ultrasonic shear wave anti-icing system for helicopter rotor blades[C]//Proceedings of the American Helicopter Society 62nd Annual Forum. Montreal, Canada: AHS, 2006.
- [48] LI D, CHEN Z. Ultrasonic vibration for instantaneously removing frozen water droplets from cold vertical surface[C]//Proceedings of the International Symposium on Heating, Ventilation and Air Conditioning. [S.l.]: Springer, 2014.
- [49] WANG Y, XU Y, SU F. Damage accumulation model of ice detach behavior in ultrasonic de-icing technology [J]. *Renewable Energy*, 2020, 153: 1396-1405.
- [50] GUO W, DONG X, LI Y, et al. Simulations on vibration mode and distribution of shear stress for icing aluminum plate excited by ultrasonic vibration[J]. *Advances in Mechanical Engineering*, 2020, 12(3): 1687814020911231.

**Acknowledgements** This work was funded by the Key Laboratory of Icing and Anti/de-icing of CARDC (No. IADL20220105) and the National Natural Science Foundation of China (No.52006107).

**Authors** Dr. SHANG Yuhe received her B.S. and M.S. degrees from Northwestern Polytechnical University, Xi'an, China, in 2012 and 2015, respectively, and her Ph.D. degree from Hong Kong University of Science and Technology in 2019. From July 2019, she works as the lecture in the School of Energy and Mechanical Engineering, Nanjing Normal University. Her main research interests include the heat and mass transfer in phase change process, functional material manufactory and computational fluid dynamics.

Prof. LI Dong received his B.S. degree from Yantai University, China, in 2007, and his Ph.D. degree from Southeast University in 2014. From July 2018, he works as an associate professor in the School of Energy and Mechanical Engineering, Nanjing Normal University. His main research interests include interface phenomena and enhancement of heat transfer, droplet impact dynamics, data center liquid cooling systems and smart management of integrated energy system.

**Author contributions** Dr. SHANG Yuhe contributed to the design and preparation of the material, conducted the analysis, interpreted the results, and wrote the manuscript. Prof. LI Dong guided the research, designed the article structure and revised the manuscript. Mr. WANG Jiayong, and Mr. SHEN Leihu conducted the experiments and data reduction. Mr. AI Fanbiao and Mr. WU Jiulong contributed to the discussion and background of the study. All authors commented on the manuscript draft and approved the submission.

**Competing interests** The authors declare no competing interests.

(Production Editor: SUN Jing)

## 防除冰过程中的传热传质特性

商雨禾<sup>1,2,3</sup>, 李 栋<sup>1,2,3</sup>, 王佳勇<sup>1</sup>, 沈雷虎<sup>1</sup>, 艾凡彪<sup>1</sup>, 吴九龙<sup>1</sup>

(1. 南京师范大学能源与机械工程学院, 南京 210046, 中国;

2. 南京师范大学江苏省能源系统过程转化与减排技术工程实验室, 南京 210046, 中国;

3. 中国空气动力研究与发展中心结冰与防除冰重点实验室, 绵阳 621000, 中国)

**摘要:**通过数值模拟和实验研究了抑制冰形成的两种方法:被动的表面功能化和主动的超声振动技术。由于表面凸起的宏观结构能在液滴扩展和收缩过程中改变其形状,因此液滴撞击具有立方体、单个和交叉三角脊以及悬空棱镜等宏观结构的超疏水表面时的接触时间可以有效降低。受到超声振动的基板会形成非线性的等效剪切应力分布,从而导致撞击液滴出现不同的动力学模式,并提高了除冰性能。研究揭示了表面宏观结构和超声振动技术对抗冰和除冰的有效性,为设计和优化抗冰/除冰系统提供了潜在方法。

**关键词:**防冰;除冰;液滴撞击;超声振动;超疏水表面;宏观结构;除霜